energies

MDPI

Article

Microstructure-Dependent Macroscopic Electro-Chemo-Mechanical Behaviors of Li-Ion Battery Composite Electrodes

Ying Zhao *, Zhongli Ge and Zongli Chen

School of Aerospace Engineering and Applied Mechanics, Tongji University, Shanghai 200092, China
* Correspondence: 19531@tongji.edu.cn

Abstract: The rapid development of the electric vehicle industry has created an urgent need for high-performance Li-ion batteries. Such demand not only requires the development of novel active materials but also requires optimized microstructure of composite electrodes. However, due to complicated heterogeneous electrode microstructure, there still lacks a relationship between the electrode microstructure and the macroscopic electro-chemo-mechanical performance of the battery. In this study, electrochemical and mechanical multi-scale models are developed in order to account for the influence of the heterogeneous microstructure on the macroscopic mechanical and electrochemical behavior of the battery. It is found that porosity and particle size are two important parameters to characterize the microstructure that can affect the macroscopic mechanical and electrochemical behavior. The models developed in this study can be served as designing guidelines for the optimization for the Li-ion battery composite electrodes.

Keywords: Li-ion battery; microstructure; multi-scale modeling; electro-chemo-mechanical coupling

check for updates

Citation: Zhao, Y.; Ge, Z.; Chen, Z. Microstructure-Dependent Macroscopic Electro-Chemo-Mechanical Behaviors of Li-Ion Battery Composite Electrodes. *Energies* **2024**, *17*, 4607. https://doi.org/10.3390/en17184607

Academic Editors: Antonino S. Aricò and JongHoon Kim

Received: 13 August 2024
Revised: 1 September 2024
Accepted: 12 September 2024
Published: 13 September 2024

Copyright: © 2024 by the authors. Licensee MDPI, Basel, Switzerland. This article is an open access article distributed under the terms and conditions of the Creative Commons Attribution (CC BY) license (https://creativecommons.org/licenses/by/4.0/).

1. Introduction

The development of the Li-ion battery industry has created unprecedented opportunities and challenges at the same time. Therefore, to develop high-performance Li-ion batteries with high energy and power density is of great importance [1]. It is well recognized that the performance of the battery is not only influenced by the active material but also by the electrode microstructure [2–6]. The success of new electrode materials lies in the optimized combination of factors such as energy density, power density, electrochemical stability, safety, material cost, and preparation process, which inevitably demands an extremely long time and great experimental efforts. On the other hand, the existing electrode materials (such as NMC) have a high theoretical capacity and power density but cannot perform their best rate capability due to the randomly designed microstructure of the composite electrode. Therefore, it is practical and effective to design optimized electrode microstructure based on the existing material system in order to improve the performance of Li-ion batteries.

It is widely studied that structural change such as cracks at the particle level can cause severe capacity fade and battery failure [7–10]. However, the structure characteristics at the electrode level have not been understood in depth due to complicated heterogeneous electrode microstructure. As a matter of fact, it has been experimentally proved that battery performances, including capacity, Coulombic efficiency, cyclic stability, and rate capability, are all greatly affected by, among other factors, particle size distribution, shape, electrode thickness, and porosity, which are characteristic at the electrode scale [11]. These characteristics can be categorized into two groups: those that represent homogeneous characteristics such as porosity and average particle size and those that represent heterogeneous characteristics such as particle size polydispersity and tortuosity.

As one of the important parameters in the microstructure of porous electrodes, porosity has been widely investigated in the literature. Introduction of more pores and increasing

porosity can improve electrode transport behavior, decrease ionic resistance, reduce polarization, and elevate the average battery potential. However, in this way, the electrode capacity will be reduced, and the mechanical stiffness and strength will be lowered. This dilemma urgently requires the delicate design of porosity in order to improve battery performance. Apart from porosity, particle size also contributes greatly to the mechanical and electrochemical performance of the batteries. It has been shown that particle size is to a great extent related to aging and degradation behaviors [12,13].

In addition to these homogeneous characteristics, the effect of microstructure heterogeneity on battery performance can also not be underestimated. The spatial distribution of each component in the electrode microstructure is proved to have a significant impact on battery performance [14–16]. Structures with smaller pore size or unevenly distributed pores usually come with high tortuosity, which can potentially give rise to longer ionic diffusion paths and higher resistance. This influence is more obvious in thick electrodes with high C-rates. Therefore, the heterogeneous electrochemical mass transfer along the electrode thickness direction should be fully considered in order to achieve accurate estimation of battery performance.

Therefore, it is important to build models that can capture both homogeneous and heterogeneous characteristics of the composite electrodes. As a straightforward approach, the heterogeneous models reconstructed based on X-ray computed tomography images are widely employed by researchers [17–21]. However, due to the experimental cost, the number of these models are limited; thus, they cannot reflect statistical characteristics of the composite electrode. Thus, computed models are developed such as coarse-grained molecular dynamics model, multi-phase smoothed particle model and discrete element method [22–27]. In order to capture the macroscopic mechanical behavior, it is common practice to employ homogenized models such as the Mori–Tanaka method [28–30].

However, there lacks a thorough investigation into the influence of these parameters because most of the models are either based on heterogeneous models that lose the statistical characteristics or on homogeneous models that lose local information. In this study, electrochemical and mechanical multi-scale models are developed in order to account for the influence of the heterogeneous and homogeneous characteristic of electrode microstructure on the macroscopic behavior of the battery. The remainder of the article is organized as follows: In Section 2, mathematical models are developed based on our previous work. For improved understanding, both heterogeneous and homogeneous models are developed and compared against each other. Numerical simulations are carried out in Section 3, where it is found that porosity and particle size are two important parameters to characterize the microstructure that can affect the macroscopic mechanical and electrochemical behavior. The models developed in this study can be served as design guidelines for the optimization of Li-ion battery composite electrodes.

2. Mathematical Models

For simplicity, we focus our study on a half-cell with lithium metal as the anode, porous polymer as the separator, and a composite cathode. The composite cathode has a porous structure mainly composed of active particles (NMC), a carbon-binder domain (CBD), and pores, which are filled with electrolyte materials. As a homogenized model, the active layer of composite cathode is simplified as a particle-reinforced composite material with active particles as the reinforcement material and the smeared-out domain of the combination of the CBD and pores as the matrix.

2.1. Heterogeneous Model

We first investigate a heterogeneous model that resolves the microstructure of the composite cathode, as shown in Figure 1. It is true that 3D heterogeneous models are more suitable for the correct prediction of electrochemical performance of composite electrodes. However, due to limited computational resources, 3D models are only able to contain a limited number of particles, losing a more general study on the overall performance

of the electrode. Therefore, in this study, only 2D structures are modeled. As for the mechanical response, since the structure is assumed sufficiently thick perpendicular to the plane concerned in the model, the plane strain assumption is employed, i.e., the out-of-plane strain vanishes. As an illustrative example, we use NMC111 as the target active material, but the knowledge gained from this study can be easily transferred to other material systems. Also, in the model, since the liquid can have a negligible influence on the mechanical performance of the electrode, we only distinguish liquid from solid electrolyte with the elastic modulus. For this particular example, a liquid electrolyte is employed. Note that the matrix has a porous structure; therefore, the quantities of the matrix are homogenized effective parameters. It is important to consider the heterogeneous structure of CBD in cases such as local fracture in the CBD or electronic conductivity of the CBD. However, in the case discussed in this work, neither electronic conductivity nor the fracture of CBD is the limiting factor of the application of the battery. Therefore, we disregarded the heterogeneous structure and employed a homogeneous CBD model for the sake of simplicity. Then, we build the electro-chemo-mechanical model of the particle and the matrix from our previous work [1,4,31] and briefly summarize here as follows.

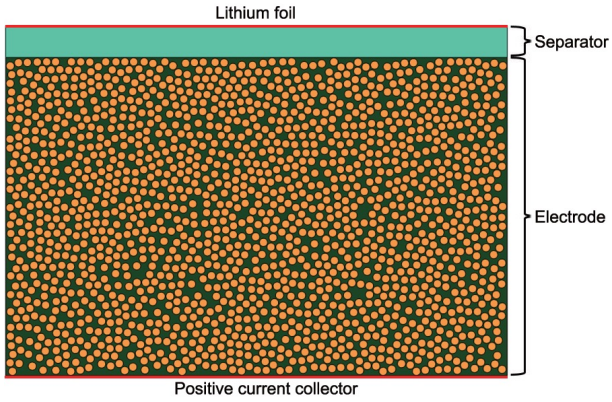


Figure 1. Schematic of the half-cell, which has a lithium metal anode, a polymer separator, and a composite cathode.

We denote the particle and matrix with the superscript p and m, respectively. In both the particle domain B^p and matrix domain B^m, there are three sets of coupled fields: the displacement field $\mathbf{u}^i$, the concentration field c^i, and the electric potential ϕ^i, where $i = p, m$. The interface between the particle and the matrix is denoted by $\Gamma^* = B^p \cap B^m$.

Mechanically, force balances are enforced in both domains:

$$\boldsymbol{\nabla} \cdot \boldsymbol{\sigma}^i = 0 \quad \text{in } B^i \tag{1}$$

where linear elastic constitutive and linear kinematic relations for both the particle and matrix are assumed.

$$\boldsymbol{\sigma}^i = \mathbb{C}^i \left(\boldsymbol{\varepsilon}^i - \frac{1}{3} \Omega^i c^i \mathbf{I} \right) \tag{2}$$

$$\boldsymbol{\varepsilon}^i = \frac{1}{2} \left(\boldsymbol{\nabla} \mathbf{u} + \boldsymbol{\nabla} \mathbf{u}^{\mathrm{T}} \right). \tag{3}$$

In the constitutive equations, we assume that both the particle and matrix are isotropic, and the expansion upon insertion of Li-ion is also isotropic; thus, the partial molar volumes Ω^i are scalars. If we use the shear modulus G^i and bulk modulus K^i to describe the material stiffness, the fourth-order stiffness tensor becomes

$$\mathbb{C}^i = 2G^i \mathbb{I} + \left(K^i - \frac{2}{3} G^i \right) \mathbf{I} \otimes \mathbf{I} \tag{4}$$

where $\mathbb{I}$ and $\mathbf{I}$ are fourth-order and second-order unit tensors, respectively. At the interface Γ^*, the compatibility conditions are enforced, viz.,

$$\mathbf{u}^p - \mathbf{u}^m = 0 \tag{5}$$

$$\boldsymbol{\sigma}^p \boldsymbol{n}^* - \boldsymbol{\sigma}^m \boldsymbol{n}^* = 0 \tag{6}$$

with $\boldsymbol{n}^*$ being the normal vector of Γ^* pointing towards the matrix. Note that in the simulation we assume the volumetric change of the matrix upon insertion/extraction of Li-ion is negligible, which yields $\Omega^m = 0$.

Electrically, we assume that the particle is electronic conductive with the particle is electronic conductive with the equilibrium potential $\phi^p = \phi^p_{\text{eq}}$, and the electric potential in the matrix follows Ohm's law

$$\boldsymbol{\nabla} \cdot \boldsymbol{i}^m = 0 \quad \text{in } B^m \tag{7}$$

where $\boldsymbol{i}^m$ is the Li^+ ionic current density in the matrix, defined by

$$\boldsymbol{i}^m = -\kappa^m \boldsymbol{\nabla} \phi^m + \left(\frac{2\kappa^m RT}{F} \right) (1 - t_+) \boldsymbol{\nabla} \ln c^m. \tag{8}$$

Here, κ^m, t_+, F, R, T denote conductivity, Li^+ transference number, the Faraday constant, the gas constant, and absolute temperature, respectively. Equation (8) implies that the current density has two driving forces: the applied electric field (first term) and the electric field induced by space charges (second term). We assume that the potential is not influenced by the reaction of the particles locally, meaning there is no interface conditions for the electric field. Instead, boundary conditions at the interfaces at the separator Γ_s and the current collector Γ_{cc} sides are imposed for the electric field. For a galvanostatic charge condition of current density $\hat{i}$, the boundary conditions are

$$\boldsymbol{i}^m \cdot \boldsymbol{n}_s = \hat{i} \quad \text{on } \Gamma_s, \tag{9}$$

$$\boldsymbol{i}^m \cdot \boldsymbol{n}_{cc} = \hat{i} \quad \text{on } \Gamma_{cc}. \tag{10}$$

Chemically, the mass conservation law governs the evolution of Li-ion concentration:

$$\frac{\partial c^i}{\partial t} = -\boldsymbol{\nabla} \cdot \mathbf{j}^i \quad \text{in } B^i \tag{11}$$

where $\mathbf{j}^p$ and $\mathbf{j}^m$ are Li-ion fluxes in the two respective domains. In the particle, we assume that the particle is electronic conductive with the equilibrium potential $\phi^p = \phi^p_{\text{eq}}$ and the stress-assisted diffusion is negligible. Thus, the Li-ions are purely driven by the concentration gradient, and the flux is given by

$$\mathbf{j}^p = -D^p \boldsymbol{\nabla} c^p \tag{12}$$

with D^p being the diffusivity of Li-ions in the active particles. In the matrix, again, we disregard the influence from the stresses on the diffusion; however, the migration due to electric potential is non-negligible. Therefore, the flux is given by

$$\mathbf{j}^m = -D^m \boldsymbol{\nabla} c^m + \frac{t_+}{F} \boldsymbol{i}^m \tag{13}$$

where D^m is the diffusivity and the current density $\boldsymbol{i}^m$ is given by Equation (8). This equation indicates that there are two contributions to the flux: the diffusion due to concentration gradient (first term), and the migration due to electric field (second term). At the interface, the current density across the interface is dictated by the Butler–Volmer equation

$$\mathbf{j}^p \cdot \boldsymbol{n}^* = j_{\text{BV}} \tag{14}$$

$$\mathbf{j}^m \cdot \boldsymbol{n}^* = j_{\mathrm{BV}} \tag{15}$$

where

$$j_{\mathrm{BV}} = i_0 \left[\exp\left(\frac{\alpha_a F \eta}{RT} \right) - \exp\left(\frac{-\alpha_c F \eta}{RT} \right) \right]. \tag{16}$$

Here, i_0 is the exchange current density,

$$i_0 = i_{0,ref} \left(\frac{c^p}{c^p_{\max}} \right)^{\alpha_c} \left(1 - \frac{c^p}{c^p_{\max}} \right)^{\alpha_a} \left(\frac{c^m}{c^m_{\mathrm{ref}}} \right) \tag{17}$$

where $i_{0,\mathrm{ref}}$, $c^p_{\max}$, c^m_{ref}, α_a and α_c are the reference exchange current density, maximum Li^+ in the particle, reference Li^+ concentration in the matrix, and the anodic and cathodic reaction factors, respectively. η is the overpotential, defined as

$$\eta = \phi^p - \phi^e - E_{\mathrm{eq}} \tag{18}$$

where E_{eq} is the equilibrium potential.

2.2. Homogeneous Model

In this section, we further smear out the particles in the matrix and consider the composite cathode as a homogeneous material with homogenized parameters to characterize statistically the microstructure, as shown in Figure 2.

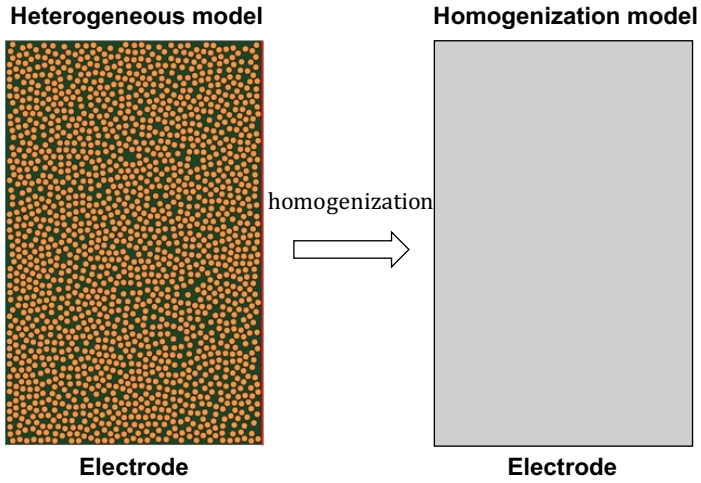


Figure 2. Schematic of homogenization of the composite electrode.

Mechanically, we consider the electrode as a particle reinforced composite, whose reinforcement is the active material NMC, and the matrix is the homogenized material of electrolyte and CBD. For the homogenized electrode, the mechanical governing equation in the cathode domain B^H is given as

$$\nabla \cdot \boldsymbol{\sigma} = 0 \quad \text{in } B^H. \tag{19}$$

As for the constitutive relation, the key is to find out effective stiffness tensor $\mathbb{C}_{\mathrm{eff}}$ and effective chemical strain $\boldsymbol{\varepsilon}^*$ such that

$$\boldsymbol{\sigma} = \mathbb{C}_{\mathrm{eff}}(\boldsymbol{\varepsilon} - \boldsymbol{\varepsilon}^*). \tag{20}$$

In order to obtain the effective stiffness, we employ the Mori–Tanaka approach [32,33]. We assume that the composite electrode as a dilute dispersion of active particles which are distributed randomly inside the electrode, where interactions between the particles

are considered through mean-field theory, as shown in Figure 3. The volume fraction of the active particles is denoted by φ. Under uniform far-field uniform stress and strain boundary conditions, we can obtain the effective stiffness tensor $\mathbb{C}_{\text{eff}}$

$$\mathbb{C}_{\text{eff}} = 2G_{\text{eff}}\mathbb{I} + \left(K_{\text{eff}} - \frac{2}{3}G_{\text{eff}}\right)\mathbf{I} \otimes \mathbf{I} \tag{21}$$

where

$$G_{\text{eff}} = G^m + \frac{\varphi(G^p - G^m)}{1 + 4(1-\varphi)G^{me}(G^p - G^m)} \tag{22}$$

$$K_{\text{eff}} = K^m + \frac{\varphi(K^p - K^m)}{1 + 9(1-\varphi)K^{me}(K^p - K^m)} \tag{23}$$

with

$$K^{me} = \frac{1}{3(4G^m + 3K^m)}, \quad G^{me} = \frac{3(2G^m + K^m)}{10G^m(4G^m + 3K^m)}. \tag{24}$$

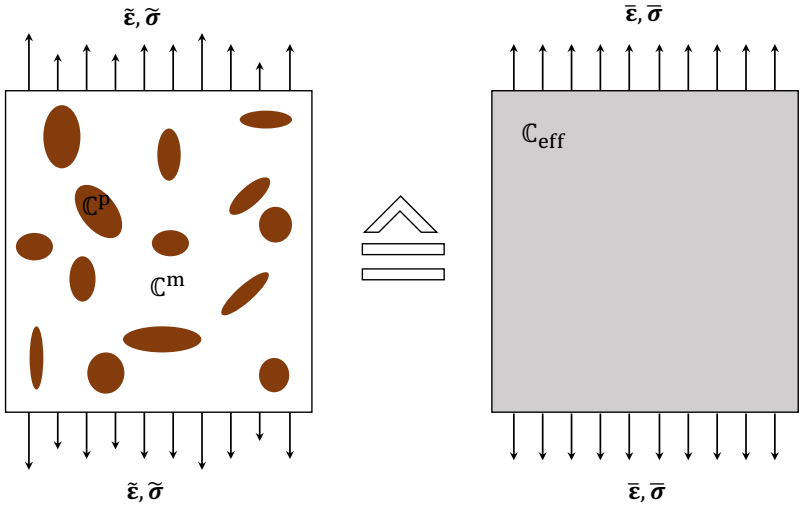


Figure 3. Schematic of homogenization of the composite electrode for the calculation of mechanical constitutive relations.

As for the macroscopic equivalent chemical strain $\boldsymbol{\varepsilon}^*$, we also perform mean-field theory and obtain

$$\boldsymbol{\varepsilon}^* = \varphi\boldsymbol{\varepsilon}_c^p + \varphi\left[(\mathbb{C}^p)^{-1} - (\mathbb{C}^m)^{-1}\right]\mathbf{b}^p \tag{25}$$

where

$$\mathbf{b}^p = (\mathbb{I} - \mathbb{B}^p)\left[(\mathbb{C}^m)^{-1} - (\mathbb{C}^p)^{-1}\right]^{-1}\boldsymbol{\varepsilon}_c^p \tag{26}$$

$$\mathbb{B}^p = \mathbb{B}^D\left[(1-\varphi)\mathbb{I} + \varphi\mathbb{B}^D\right]^{-1} \tag{27}$$

$$\mathbb{B}^D = \mathbb{C}^p\left[\mathbb{I} + \mathbb{S}(\mathbb{C}^m)^{-1}(\mathbb{C}^p - \mathbb{C}^m)\right]^{-1}(\mathbb{C}^m)^{-1}. \tag{28}$$

Here, $\boldsymbol{\varepsilon}_c^p$ is the chemical strain of the particle, and we disregard the chemical strain of the matrix. $\mathbb{S}$ is the fourth-order Eshelby tensor, which is a function of particle shape and matrix Poisson's ratio.

Electrochemically, we further disregard the variation along the direction parallel to the separator and only consider the variation along the thickness direction, which is denoted

by X. In this way, we come to the modified P2D formulation, where the key parameter is the effective diffusivity D_{eff} and effective conductivity κ_{eff} and are obtained from the microstructure [34]. Based on our previous work [15], we use the volume fraction of active particle φ and the tortuosity τ to estimate the effective transport coefficients in the matrix

$$D_{\text{eff}} = \frac{1-\varphi}{\tau} D^m \tag{29}$$

$$\kappa_{\text{eff}} = \frac{1-\varphi}{\tau} \kappa^m. \tag{30}$$

With the effective transport coefficient, we can write our electrochemical model as following, the more detailed model can be found in our previous work [35,36]. In the absence of the mechanical interactions between the particle and the matrix, there are two sets of coupled fields concerned in this model: the Li-ion concentration c^i and the electric potential φ^i where $i = p, m$. The Li^+ can only flow in the matrix, contributing to the electric field in the matrix; the electrons are supposed to flow within the particle networks, contributing to the electric field inside the particle phase. Thus, given the thickness of the cathode as L, the governing equations for the electrochemical coupling of the two phases

$$(1-\varphi)\frac{\partial c^m}{\partial t} = D_{\text{eff}}\frac{\partial^2 c^m}{\partial X^2} - \frac{t_+}{F}\frac{\partial i^m}{\partial X} + \left(1 - t_+^0\right) J_{\text{eff}} \quad (0 < X < L) \tag{31}$$

$$\frac{\partial i^p}{\partial X} + F J_{\text{eff}} = 0 \quad (0 < X < L) \tag{32}$$

$$\frac{\partial i^m}{\partial X} - F J_{\text{eff}} = 0 \quad (0 < X < L) \tag{33}$$

where J_{eff} is the wall flux, representing the reaction at the particle/matrix interface

$$J_{\text{eff}} = a j_{\text{BV}}. \tag{34}$$

Here, a is the specific surface area per unit volume, which is related to the particle size, shape, and volume fraction. j_{BV} is the flux due to the Butler–Volmer reaction at the interface, given by Equation (16). t_+ is the transference number, as explained in the last section. The current densities at the particle and matrix phases are given by

$$i^p = -\kappa^p \frac{\partial \varphi^p}{\partial X} \tag{35}$$

$$i^m = -\kappa_{\text{eff}}\frac{\partial \varphi^m}{\partial X} + \left(\frac{2\kappa_{\text{eff}} RT}{F}\right)(1 - t_+)\frac{\partial \ln c^m}{\partial X}. \tag{36}$$

As for the boundary conditions at the electrode/separator interface, flux boundary conditions can be specified for galvanostatic boundary conditions; at the electrode/current collector interface, no flux of Li^+ is allowed since it is not permeable to ions. For a more specific discussion, please refer to our previous work [35].

3. Results and Discussion

In this section, composite electrodes with different particle sizes and volume fractions are constructed, both with heterogeneous and homogeneous models, and the mechanical and electrochemical behavior variations between different microstructures are discussed. The parameters used in this study are given in Table 1.

Table 1. Parameters of the particle packing electrode model used in the simulation.

Definition of Parameters	Symbol (Unit)	Value
Electrode thickness	L (µm)	237
Maximum concentration of Li^+ of active material	c^p_{max} (mol m^{-3})	49,500
Li^+ diffusion coefficient in matrix	D^m (m^2 s^{-1})	Equation (37)
Li^+ conductivity in matrix	κ^m (S m^{-1})	Equation (38)
Li^+ diffusion coefficient in NMC111 particles	D^p (m^2 s^{-1})	3×10^{-14}
Initial concentration of Li+ in electrolyte	C_0 (mol m^{-3})	1000
Transference number of Li	t_+	0.363
Transfer coefficients	α_a, α_c	0.5
Temperature	T (K)	298
Young's modulus of NMC particles	E^p (GPa)	78
Poisson's ratio of NMC particles	ν^p	0.25
Young's modulus of matrix *	E^m(GPa)	5
Poisson's ratio of matrix *	ν^m	0.25

* Mixture of electrolyte (volume fraction 70%) and CBD (volume fraction 30%).

In addition, the diffusivity D^m and conductivity κ^m of the matrix are given as a function of Li^+ concentration This is example 2 of equation:

$$D^m = 7.588 \times 10^{-11}(c^m)^2 - 3.036 \times 10^{-10}c^m + 3.654 \times 10^{-10} \quad (37)$$

$$\sigma^m = 1.2544 \times 10^{-4}c^m \times \left[-8.2488 + 5.3248 \times 10^{-2}T - 2.987 \times 10^{-5}T^2 + 2.6235 \times 10^{-4}c^m - 9.3063 \times 10^{-6}c^m T + 8.069 \times 10^{-9}c^m T^2 + 2.2002 \times 10^{-7}(c^m)^2 - 1.765 \times 10^{-10}(c^m)^2 T\right]^2 \quad (38)$$

3.1. Mechanical Behavior

As a first example, we examine the effective stiffness in the composite electrode, which is reinforced with spherical particles of three different radii: 3 µm, 6 µm, and 9 µm. For the heterogeneous model, we impose a uniaxial tension test on the electrode as shown in Figure 4 and calculate the effective Young's modulus E_{eff}.

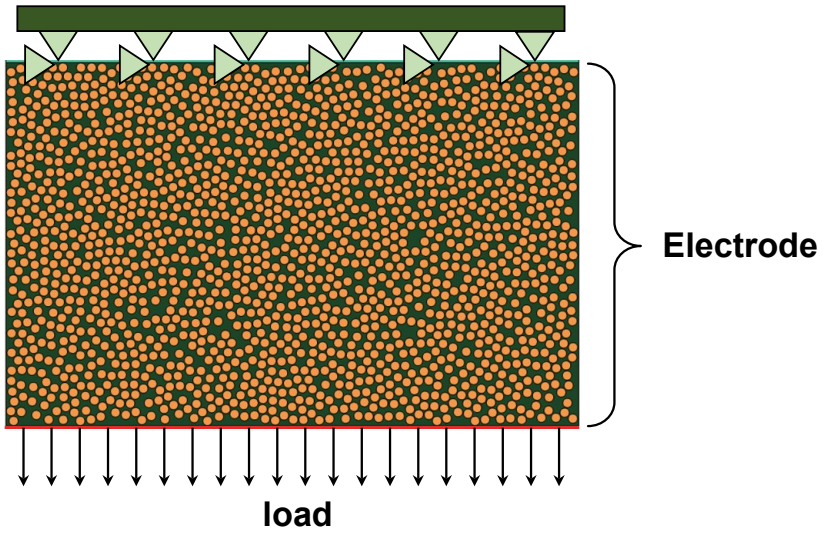


Figure 4. Schematic of the uniaxial loading test for the calculation of Young's modulus of the composite electrode.

As for the homogeneous model, we can immediately obtain effective bulk and shear moduli from Equations (22) and (23) and calculate the effective Young's modulus from the relation

$$E_{\text{eff}} = \frac{9K_{\text{eff}}}{1 + \frac{3K_{\text{eff}}}{G_{\text{eff}}}}. \tag{39}$$

The results are shown in Figures 5–7. We can see that results from heterogeneous model agree very well with the homogeneous model, and for all three cases, the increase in the particle volume fraction gives rise to enhanced stiffness. Furthermore, both heterogeneous and homogeneous models show that particle size play negligible roles in influencing effective macroscopic stiffness of the composite cathode. This can be explained by the fact that volume fraction, rather than local arrangements of the microstructure, plays a dominant role in the macroscopic properties. However, as shown in the contour plots of the heterogeneous models in Figures 5–7, particle size plays a key role in local stress state in the composite cathodes. It is obvious that electrodes with smaller particles generally have lower average stresses with smaller fluctuations; electrodes with larger particles suffer from more severe stress concentration and are thus more vulnerable to fracture. This phenomenon shows that smaller particles are generally distributed more uniformly inside the electrode, each bearing similar loads with each other. However, larger particles tend to distribute less uniformly, which leads to higher fluctuations in the loads each particle takes.

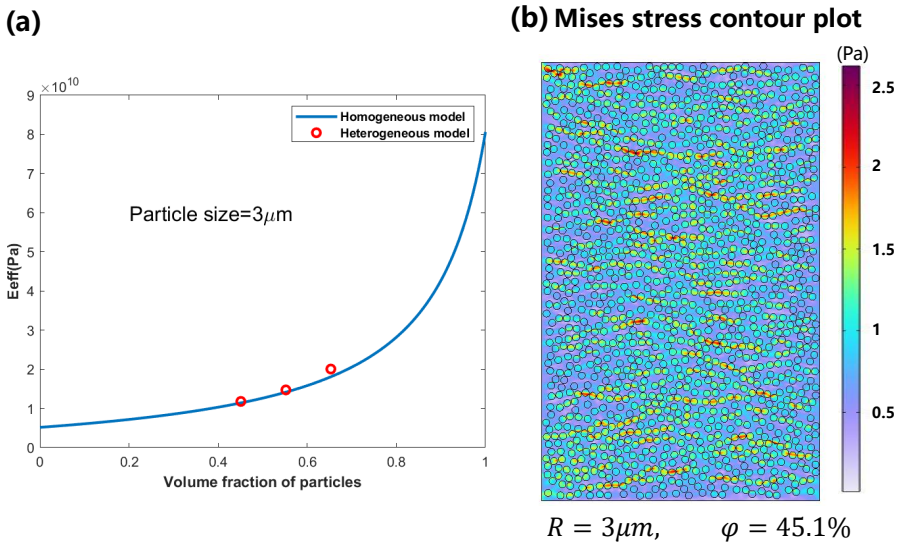


Figure 5. Effective modulus of the composite electrode with particle size $r = 3\,\mu\text{m}$. (**a**) Effective modulus against volume fraction of particles (φ). (**b**) Contour plot of von Mises stress for the volume fraction $\varphi = 45.1\%$ under a uniaxial loading of $1\,\text{N}\,\text{m}^{-2}$.

We also plotted the macroscopic chemical strain with different volume fractions as shown in Figure 8. It is shown that, in general, more loading of active particles—a higher particle volume fraction—gives rise to increased macroscopic chemical strain. Particle size again plays a negligible role in influencing this strain. The deviation of case for small particles at low volume fraction can be explained by the fact that, in such particular case, the size of particles are comparable with that of the gaps, which may allow rigid-body movements of particles to accommodate volume expansion of particles, resulting a slightly smaller macroscopic volume expansion. As for the stresses, as shown in Figure 8b,c, higher loading of particles will give rise to a more uniformly distributed stress field, which is beneficial in resisting chemical strain-induced cracks.

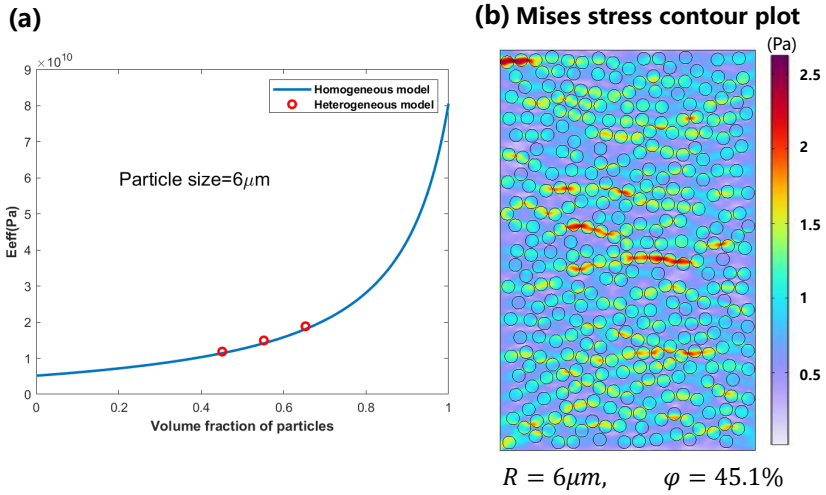


Figure 6. Effective modulus of the composite electrode with particle size $r = 6\,\mu\text{m}$. (**a**) Effective modulus against volume fraction of particles (φ). (**b**) Contour plot of von Mises stress for the volume fraction $\varphi = 45.1\%$ under a uniaxial loading of $1\,\text{N}\,\text{m}^{-2}$.

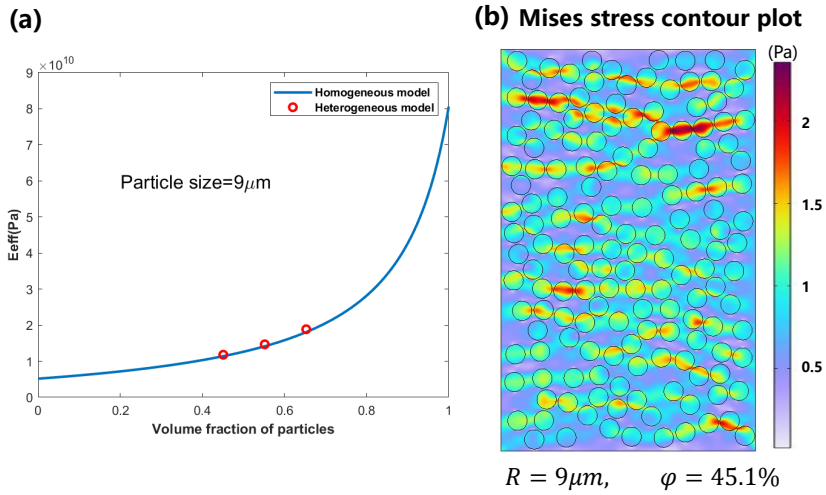


Figure 7. Effective modulus of the composite electrode with particle size $r = 9\,\mu\text{m}$. (**a**) Effective modulus against volume fraction of particles (φ). (**b**) Contour plot of von Mises stress for the volume fraction $\varphi = 45.1\%$ under a uniaxial loading of $1\,\text{N}\,\text{m}^{-2}$.

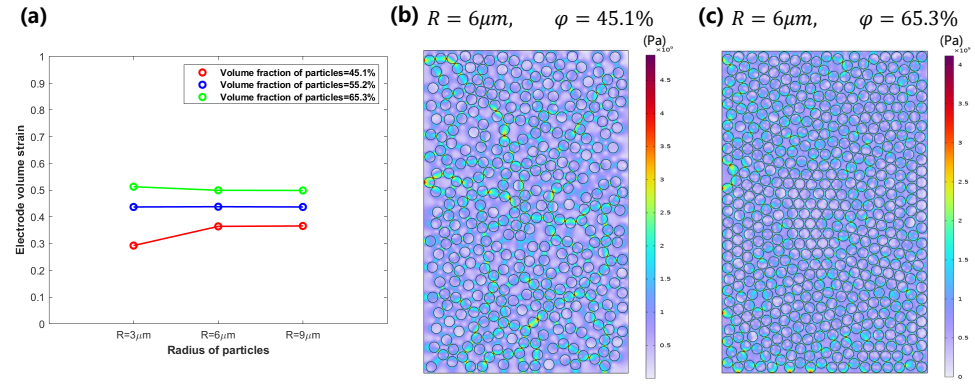


Figure 8. (**a**) Variation in relative macroscopic chemical strain $\varepsilon^*/\varepsilon_c^p$ against particle size and volume fraction. The von Mises stress for a particle size of 6 µm with volume fraction (**b**) $\varphi = 45.1\%$ and (**c**) $\varphi = 65.3\%$ under particle chemical strain $\varepsilon_c^p = 0.3$.

3.2. Electrochemical Behavior

As a last example, we would like to know how electrode microstructure can influence the electrochemical performance of the composite electrode. We integrate the cathode into a half-cell and run galvanostatic discharge until a cut-off voltage of 2.5 V. Figure 9a shows the discharge curve estimated by both heterogeneous and homogeneous (P2D) models, both of which agree well with experimental results. Furthermore, in order to evaluate the rate performance, we test the three different cells under different C-rates and measure the depth of discharge (DOD) curves against the particle volume fraction. The results are shown in Figure 9b–d. It is shown that the DOD decreases drastically with increased loading of the active materials. This is an indication that increasing the amount of active material will not necessarily bring about increased capacity. On the contrary, excessive active materials will do harm to the accessible capacity, especially at high discharge rates. Furthermore, the results also show that electrodes with smaller particles generally show much a better rate capability, even with high loading of active materials. The reason for this is that in the battery with liquid electrolyte and NMC particles, the limiting factor of the charge/discharge rate is mostly solid diffusion inside the particles. Therefore, enhancement of particle diffusion efficiency will greatly enhance the rate capability of the complete battery. It should, however, also be noted that in this model we disregard side reactions such as solid-electrolyte-interphase (SEI) formation, which probably favors less exposed surfaces per unit volume, i.e., larger particles, in order to minimize the consumption of lithium and to elongate the lifespan. For these models, the readers are referred to degradation models such as Zhu et al. [37].

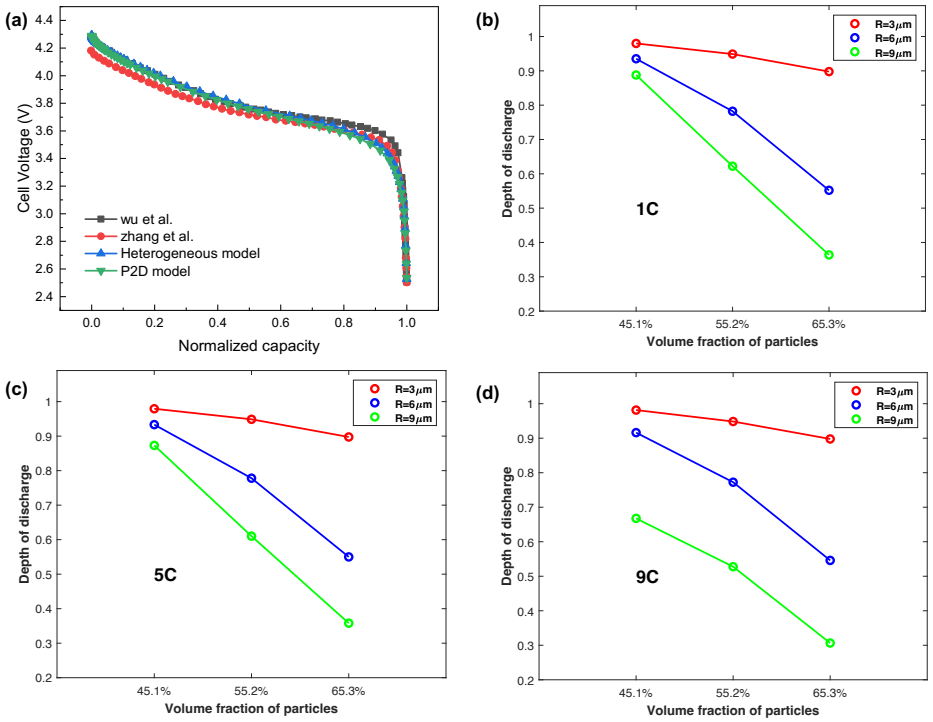


Figure 9. The electrochemical performance of the composite cathode. (**a**) Discharge curve with different models compared to experimental results conducted by Wu et al. [38] and Zhang et al. [39]. The depth of discharge (DOD) curve against particle size and volume fraction with galvanostatic discharge of (**b**) 1C, (**c**) 5C and (**d**) 9C conditions.

The reason is shown in Figure 10, which shows that electrodes with smaller particles in general have more uniform Li^+ concentration distribution in both the matrix and in the particle, leading to more efficient usage of active material capacity. This conclusion encourages the employment of smaller particles in the composite cathode.

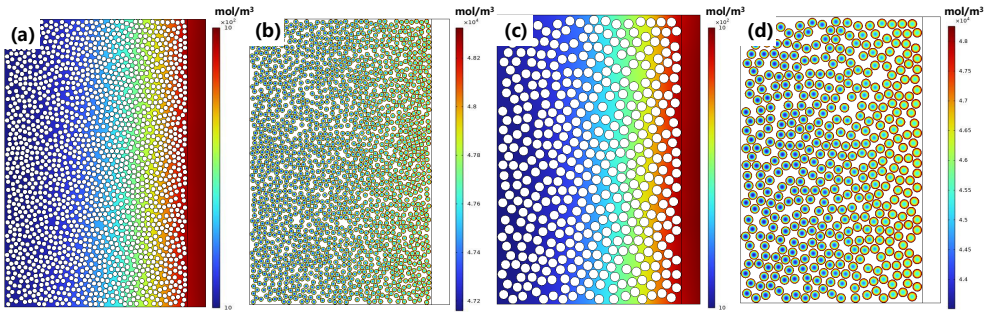


Figure 10. Concentration distribution (**a**) in matrix (particle size $r = 3\,\mu m$), (**b**) in particles (particle size $r = 3\,\mu m$), (**c**) in matrix (particle size $r = 6\,\mu m$) and (**d**) in particles (particle size $r = 6\,\mu m$) under 1C galvanostatic discharge.

4. Conclusions

In this study, electrochemical and mechanical multi-scale models are developed in order to account for the influence of the heterogeneous and homogeneous characteristics of electrode microstructure on the macroscopic behavior of the battery. To obtain an improved understanding, both heterogeneous and homogeneous models are developed and compared against each other. It is found that porosity and particle size are two important parameters to characterize the microstructure that can affect the macroscopic mechanical and electrochemical behavior. Both from the mechanical and electrochemical point of view, reducing particle size is an effective way to enhance the battery performance, especially at high C-rates. The models developed in this study can be served as designing guidelines for the optimization for the Li-ion battery composite electrodes. Nonetheless, both models cannot capture the failure mechanisms such as fracture at different levels and side reactions, which may lead to discrepancies with experimental results. Therefore, it is highly important to consider failure mechanisms in the model in the future.

Author Contributions: Conceptualization, methodology, formal analysis, investigation, resources, writing—original draft preparation, writing—review and editing, supervision, project administration, funding acquisition: Y.Z.; validation, data curation, visualization: Z.G. and Z.C. All authors have read and agreed to the published version of the manuscript.

Funding: This research was funded by the National Natural Science Foundation of China (Project No. 12102305) and the Fundamental Research Funds for the Central Universities.

Data Availability Statement: The original contributions presented in the study are included in the article, further inquiries can be directed to the corresponding author.

Conflicts of Interest: The authors declare no conflicts of interest.

Abbreviations

The following abbreviations are used in this manuscript:

LIB	Lithium-ion battery
CBD	Carbon-binder domain
P2D	Pseudo two-dimensional
DOD	Depth of discharge

References

1. Zhao, Y.; Stein, P.; Bai, Y.; Al-Siraj, M.; Yang, Y.; Xu, B.X. A review on modeling of electro-chemo-mechanics in lithium-ion batteries. *J. Power Sources* **2019**, *413*, 259–283. [CrossRef]
2. Hu, Y.; Zhao, X.; Suo, Z. Averting cracks caused by insertion reaction in lithium–ion batteries. *J. Mater. Res.* **2010**, *25*, 1007–1010. [CrossRef]
3. Liu, X.H.; Zhong, L.; Huang, S.; Mao, S.X.; Zhu, T.; Huang, J.Y. Size-Dependent Fracture of Silicon Nanoparticles during Lithiation. *ACS Nano* **2012**, *6*, 1522–1531. [CrossRef]

4. Zhao, Y.; Schillinger, D.; Xu, B.X. Variational boundary conditions based on the Nitsche method for fitted and unfitted isogeometric discretizations of the mechanically coupled Cahn–Hilliard equation. *J. Comput. Phys.* **2017**, *340*, 177–199. [CrossRef]
5. Yang, Y.; Xu, R.; Zhang, K.; Lee, S.J.; Mu, L.; Liu, P.; Waters, C.K.; Spence, S.; Xu, Z.; Wei, C.; et al. Quantification of Heterogeneous Degradation in Li-Ion Batteries. *Adv. Energy Mater.* **2019**, *9*, 1900674. [CrossRef]
6. Heubner, C.; Nick, A.; Seeba, J.; Reuber, S.; Junker, N.; Wolter, M.; Schneider, M.; Michaelis, A. Understanding thickness and porosity effects on the electrochemical performance of $LiNi_{0.6}Co_{0.2}Mn_{0.2}O_2$-based cathodes for high energy Li-ion batteries. *J. Power Sources* **2019**, *419*, 119–126. [CrossRef]
7. Itou, Y.; Ukyo, Y. Performance of $LiNiCoO_2$ materials for advanced lithium-ion batteries. *J. Power Sources* **2005**, *146*, 39–44. [CrossRef]
8. Bucci, G.; Swamy, T.; Chiang, Y.M.; Carter, W.C. Random Walk Analysis of the Effect of Mechanical Degradation on All-Solid-State Battery Power. *J. Electrochem. Soc.* **2017**, *164*, A2660–A2664. [CrossRef]
9. Nam, G.W.; Park, N.Y.; Park, K.J.; Yang, J.; Liu, J.; Yoon, C.S.; Sun, Y.K. Capacity Fading of Ni-Rich NCA Cathodes: Effect of Microcracking Extent. *ACS Energy Lett.* **2019**, *4*, 2995–3001. [CrossRef]
10. Xu, R.; Yang, Y.; Yin, F.; Liu, P.; Cloetens, P.; Liu, Y.; Lin, F.; Zhao, K. Heterogeneous damage in Li-ion batteries: Experimental analysis and theoretical modeling. *J. Mech. Phys. Solids* **2019**, *129*, 160–183. [CrossRef]
11. Bläubaum, L.; Röder, F.; Nowak, C.; Chan, H.S.; Kwade, A.; Krewer, U. Impact of Particle Size Distribution on Performance of Lithium-Ion Batteries. *ChemElectroChem* **2020**, *7*, 4755–4766. [CrossRef]
12. Liang, J.; Gan, Y.; Yao, M. Numerical analysis on the aging characteristics of a $LiFePO_4$ battery: Effect of active particle sizes in electrodes. *J. Energy Storage* **2023**, *67*, 107546. [CrossRef]
13. Lee, Y.K. Effect of porous structure and morphology of cathode on the degradation of lithium-ion batteries. *J. Energy Storage* **2022**, *52*, 104788. [CrossRef]
14. Chen, Z.; Zhao, Y. A quasi-physical method for random packing of spherical particles. *Powder Technol.* **2022**, *412*, 118002. [CrossRef]
15. Chen, Z.; Zhao, Y. Tortuosity estimation and microstructure optimization of non-uniform porous heterogeneous electrodes. *J. Power Sources* **2024**, *596*, 234095. [CrossRef]
16. Baek, K.; Kim, H.; Shin, H.; Park, H.; Cho, M. Multiscale study to investigate nanoparticle agglomeration effect on electrical conductivity of nano-SiC reinforced polypropylene matrix composites. *Mech. Adv. Mater. Struct.* **2023**, *30*, 2442–2452. [CrossRef]
17. Nagda, V.; Kulachenko, A.; Lindström, S.B. Image-based 3D characterization and reconstruction of heterogeneous battery electrode microstructure. *Comput. Mater. Sci.* **2023**, *223*, 112139. [CrossRef]
18. Hein, S.; Feinauer, J.; Westhoff, D.; Manke, I.; Schmidt, V.; Latz, A. Stochastic microstructure modeling and electrochemical simulation of lithium-ion cell anodes in 3D. *J. Power Sources* **2016**, *336*, 161–171. [CrossRef]
19. Kashkooli, A.G.; Farhad, S.; Lee, D.U.; Feng, K.; Lister, S.; Babu, S.K.; Zhu, L.; Chen, Z. Multiscale modeling of lithium-ion battery electrodes based on nano-scale X-ray computed tomography. *J. Power Sources* **2016**, *307*, 496–509. [CrossRef]
20. Lu, X.; Bertei, A.; Finegan, D.P.; Tan, C.; Daemi, S.R.; Weaving, J.S.; O'Regan, K.B.; Heenan, T.M.M.; Hinds, G.; Kendrick, E.; et al. 3D microstructure design of lithium-ion battery electrodes assisted by X-ray nano-computed tomography and modelling. *Nat. Commun.* **2020**, *11*, 2079. [CrossRef]
21. Boyce, A.M.; Lu, X.; Brett, D.J.L.; Shearing, P.R. Exploring the influence of porosity and thickness on lithium-ion battery electrodes using an image-based model. *J. Power Sources* **2022**, *542*, 231779. [CrossRef]
22. Liu, C.; Arcelus, O.; Lombardo, T.; Oularbi, H.; Franco, A.A. Towards a 3D-resolved model of Si/Graphite composite electrodes from manufacturing simulations. *J. Power Sources* **2021**, *512*, 230486. [CrossRef]
23. Nikpour, M.; Barrett, N.; Hillman, Z.; Thompson, A.I.; Mazzeo, B.A.; Wheeler, D.R. A Model for Investigating Sources of Li-Ion Battery Electrode Heterogeneity: Part I. Electrode Drying and Calendering Processes. *J. Electrochem. Soc.* **2021**, *168*, 060547. [CrossRef]
24. Giménez, C.S.; Finke, B.; Schilde, C.; Froböse, L.; Kwade, A. Numerical simulation of the behavior of lithium-ion battery electrodes during the calendaring process via the discrete element method. *Powder Technol.* **2019**, *349*, 1–11. [CrossRef]
25. Ge, R.; Cumming, D.J.; Smith, R.M. Discrete element method (DEM) analysis of lithium ion battery electrode structures from X-ray tomography-the effect of calendering conditions. *Powder Technol.* **2022**, *403*, 117366. [CrossRef]
26. Fang, R.; Ge, H.; Wang, Z.; Li, Z.; Zhang, J. A Two-Dimensional Heterogeneous Model of Lithium-Ion Battery and Application on Designing Electrode with Non-Uniform Porosity. *J. Electrochem. Soc.* **2020**, *167*, 130513. [CrossRef]
27. Kim, Y.J.; Hoang, T.D.; Han, S.C.; Bang, J.A.; Kang, H.W.; Kim, J.; Park, H.; Park, J.H.; Park, J.W.; Park, G.; et al. Exploring optimal cathode composite design for high-performance all-solid-state batteries. *Energy Storage Mater.* **2024**, *71*, 103607. [CrossRef]
28. Song, K.; Lu, B.; He, Y.; Song, Y.; Zhang, J. Modulus Estimation of Composites with High Porosity, High Particle Volume Fraction, and Particle Eigenstrain: Application to the LIB Active Layer with a Bridged-Particle Mesostructure. *Energies* **2023**, *16*, 1424. [CrossRef]
29. Gudmundson, P.; Larsson, P.L. An analytic model for effective mechanical properties and local contact stresses in lithium-ion porous electrodes. *Extrem. Mech. Lett.* **2021**, *42*, 101067. [CrossRef]
30. Ücel, I.B.; Gudmundson, P. A statistical RVE model for effective mechanical properties and contact forces in lithium-ion porous electrodes. *Int. J. Solids Struct.* **2022**, *244–245*, 111602. [CrossRef]

31. Tang, W.; Chen, Z.; Zhao, Y. Assessment of Optimization Strategies for Battery Electrode-Active Particles Based on Chemomechanical Analysis. *J. Electrochem. Energy Convers. Storage* **2022**, *19*, 041001. [CrossRef]
32. Benveniste, Y. A new approach to the application of Mori-Tanaka's theory in composite materials. *Mech. Mater.* **1987**, *6*, 147–157. [CrossRef]
33. Golmon, S.; Maute, K.; Dunn, M.L. Numerical modeling of electrochemical–mechanical interactions in lithium polymer batteries. *Comput. Struct.* **2009**, *87*, 1567–1579. [CrossRef]
34. Doyle, M.; Fuller, T.F.; Newman, J. Modeling of Galvanostatic Charge and Discharge of the Lithium/Polymer/Insertion Cell. *J. Electrochem. Soc.* **1993**, *140*, 1526. [CrossRef]
35. Zhao, Y.; Deshpande, V.S.; Fleck, N.A. A compliant and low-expansion 2-phase micro-architectured material, with potential application to solid-state Li-ion batteries. *J. Mech. Phys. Solids* **2022**, *158*, 104683. [CrossRef]
36. Bai, Y.; Zhao, Y.; Liu, W.; Xu, B.X. Two-level modeling of lithium-ion batteries. *J. Power Sources* **2019**, *422*, 92–103. [CrossRef]
37. Zhu, K.; Wang, T.; Wu, Y.; Luo, J.; Huang, Y. Comprehensive aging model coupling chemical and mechanical degradation mechanisms for NCM/C6-Si lithium-ion batteries. *Energy Storage Mater.* **2024**, *71*, 103620. [CrossRef]
38. Wu, S.L.; Zhang, W.; Song, X.; Shukla, A.K.; Liu, G.; Battaglia, V.; Srinivasan, V. High Rate Capability of $Li(Ni_{1/3}Mn_{1/3}Co_{1/3})O_2$ Electrode for Li-Ion Batteries. *J. Electrochem. Soc.* **2012**, *159*, A438. [CrossRef]
39. Zhang, X.; Mauger, A.; Jiang, W.; Groult, H.; Julien, C.M. Diffusion of Li^+ Ions in $LiNi_{1/3}Mn_{1/3}Co_{1/3}O_2$. *ECS Trans.* **2011**, *35*, 89. [CrossRef]

Disclaimer/Publisher's Note: The statements, opinions and data contained in all publications are solely those of the individual author(s) and contributor(s) and not of MDPI and/or the editor(s). MDPI and/or the editor(s) disclaim responsibility for any injury to people or property resulting from any ideas, methods, instructions or products referred to in the content.